# Cascaded nanooptics to probe microsecond atomic-scale phenomena

Marlous Kamp[a,b,1,2], Bart de Nijs[a,1], Nuttawut Kongsuwan[c], Matthias Saba[c,3], Rohit Chikkaraddy[a], Charlie A. Readman[a], William M. Deacon[a], Jack Griffiths[a], Steven J. Barrow[b,4], Oluwafemi S. Ojambati[a], Demelza Wright[a], Junyang Huang[a], Ortwin Hess[c,d], Oren A. Scherman[b,2], and Jeremy J. Baumberg[a,2]

[a]NanoPhotonics Centre, Department of Physics, University of Cambridge, Cambridge, CB3 0HE, United Kingdom; [b]Melville Laboratory for Polymer Synthesis, Department of Chemistry, University of Cambridge, Cambridge, CB2 1EW, United Kingdom; [c]The Blackett Laboratory, Department of Physics, Imperial College London, London, SW7 2AZ, United Kingdom and [d]School of Physics and CRANN Institute, Trinity College Dublin, Dublin 2, Ireland

Edited by George C. Schatz, Northwestern University, Evanston, IL, and approved April 30, 2020 (received for review November 15, 2019)

**Plasmonic nanostructures can focus light far below the diffraction limit, and the nearly thousandfold field enhancements obtained routinely enable few- and single-molecule detection. However, for processes happening on the molecular scale to be tracked with any relevant time resolution, the emission strengths need to be well beyond what current plasmonic devices provide. Here, we develop hybrid nanostructures incorporating both refractive and plasmonic optics, by creating $SiO_2$ nanospheres fused to plasmonic nanojunctions. Drastic improvements in Raman efficiencies are consistently achieved, with (single-wavelength) emissions reaching $10^7$ counts·mW$^{-1}$·s$^{-1}$ and $5 \times 10^5$ counts·mW$^{-1}$·s$^{-1}$·molecule$^{-1}$, for enhancement factors $>10^{11}$. We demonstrate that such high efficiencies indeed enable tracking of single gold atoms and molecules with 17-μs time resolution, more than a thousandfold improvement over conventional high-performance plasmonic devices. Moreover, the obtained (integrated) megahertz count rates rival (even exceed) those of luminescent sources such as single-dye molecules and quantum dots, without bleaching or blinking.**

nanophotonics | nanolensing | surface-enhanced Raman scattering (SERS) | few-molecule sensing | microsecond integration times

Plasmonic structures are widely used for sensing, on account of their ability to confine light and thus create strong local electromagnetic fields (1). Tremendous effort has been devoted to designing ever-better plasmonic nanostructures to maximize these field strengths and thus improve sensing capabilities (2–5). Recently, plasmonic enhancements have been successfully combined with other types of optical confinement, such as the evanescent fields at the surfaces of whispering gallery mode resonators (6) [which have in fact also been used for plasmon-free Raman sensing (7–9)] and the interference maxima provided by Fabry–Pérot cavities (10, 11). Often, however, these nanostructures are difficult to fabricate with low yield and high cost. Few studies have exploited nanorefractive elements (12), even though nanoscale spherical lenses are already known to be capable of focusing of light beyond the diffraction limit (13–16) and can thus aid in directing incident light to optimally excite plasmonic hot spots.

Here, we show that, by combining dielectric nanooptics and plasmonic confinement through simple self-assembly methods into a single colloidal nanoarchitecture, robust and reproducible surface-enhanced Raman scattering (SERS) enhancement factors exceeding $10^{11}$ and SERS efficiencies exceeding $5 \times 10^5$ counts·mW$^{-1}$·s$^{-1}$·molecule$^{-1}$ are routinely achieved. Enhancement factors as high as $10^{14}$ will occasionally be quoted in literature, but none of these high-performance SERS substrates show efficiencies anywhere near those observed here (*SI Appendix*, *Supplementary Materials and Methods* and Table T1). The high optical efficiency and field enhancement allow for spectra to be collected at submicrowatt laser powers and provide unrivalled signal-to-noise ratios, reaching $>10^3$ to 1 for only 250-μJ laser dose. To illustrate these improved signal-to-noise ratios, we show it is now possible to detect naturally abundant $^{13}C$ isotopologues within ensembles of nonresonant molecules. Important for development of surface science, we show that a single-atom protrusion or picocavity induced in the nanogap [which further focuses the field down to a single molecule (17, 18)] allows us to track the behavior of individual nonresonant molecules and gold atoms in real time with time resolutions of tens of microseconds. This is fast enough to track single metal atom movements and resolve conformational changes in analytes, making the technique suitable for real-time monitoring of catalytic and chemical reaction processes on a single-molecule level. The obtained megahertz count rates (cts·s$^{-1}$) vie with (and even exceed) conventional luminescent sources such as single-dye

## Significance

**Surface-enhanced Raman spectroscopy (SERS) is a powerful analytical technique capable of single-molecule sensing. Here, by designing nanoarchitectures that combine nanoscale lensing and plasmonic coupling, its optical efficiency is improved a thousandfold. The intense signals we now achieve rival the brightness of conventional single-molecule fluorescent dyes and other two-level systems. We demonstrate its capability by resolving the real-time microsecond dynamics of individual gold atoms and lattice defects at room temperature. We also show the ability to detect individual isotopes within ensembles of nonresonant molecules. This step change in signal-to-noise shows the untapped potential of SERS and demonstrates its capability for direct real-time monitoring of chemistry in ambient conditions.**

Author contributions: M.K., B.d.N., R.C., and J.J.B. designed research; M.K., B.d.N., N.K., and M.S. performed research; M.K., B.d.N., O.H., O.A.S., and J.J.B. analyzed data; M.K., B.d.N., and J.J.B. wrote the paper; N.K., M.S., R.C., and O.H. performed simulations; C.A.R. performed density functional theory calculations; W.M.D. and J.G. assisted in building/programming optical setups; S.J.B. synthesized the polymer crucial for the synthesis of our gold/silica heterodimers; O.S.O., D.W., and J.H. tested reproducibility on separate setups; M.K., B.d.N., W.M.D., J.G., and S.J.B. contributed new reagents/analytic tools; and O.H., O.A.S., and J.J.B. supervised the research.

The authors declare no competing interest.

This article is a PNAS Direct Submission.



Data deposition: All relevant data present in this paper can be accessed at the University of Cambridge, https://doi.org/10.17863/CAM.52884. The source data underlying Figs. 1–4 are provided.

[1]M.K. and B.d.N. contributed equally to this work.

[2]To whom correspondence may be addressed. Email: mkamp@cantab.net, oas23@cam.ac.uk, or jjb12@cam.ac.uk.

[3]Present address: Adolphe Merkle Institute, University of Fribourg, 1700 Fribourg, Switzerland.

[4]Present address: School of Science, RMIT University, Melbourne VIC 3000, Australia.

This article contains supporting information online at https://www.pnas.org/lookup/suppl/doi:10.1073/pnas.1920091117/-/DCSupplemental.

molecules and quantum dots used for tagged and tracked emission, with the additional advantage that these Raman signals do not exhibit bleaching or blinking (19, 20).

## Results and Discussion

**Superefficient Plasmonic Nanoarchitectures for Raman Kinetics Yield Extremely High SERS Efficiencies.** The base nonhybrid SERS nanostructure used here is the nanoparticle-on-mirror (NPoM), which already delivers the highest optical confinement inside individual sub-2-nm nanogaps (21, 22). This well-established geometry (Fig. 1 *A*, *Top*) is a versatile plasmonic construct consisting of gold nanoparticles (AuNPs) deposited onto a mirror of gold (though other coinage metals also work well). A self-assembled monolayer (SAM) of analytes on the mirror surface precisely controls the size of the nanogaps and ensures that analytes are positioned at the center of the hot spots. Spacer layers are not limited to SAMs but can also consist of two-dimensional (2D) materials (23, 24), lipids (25), and rigid molecular scaffolding (26, 27). This geometry facilitates the probing of billions of optically accessible nanojunctions with nearly identical nanogaps (17, 24–31). The AuNP optically couples to its image charge below the metal surface, forming a virtual plasmonic dimer upon excitation. High-angle irradiation induces a coupled vertical dipole with field enhancements approaching three orders of magnitude, enabling ultrasensitive and single-molecule Raman sensing (17, 31–34). However, the optimal excitation and emission of this coupled mode is at 60° from normal (35), hampering efficient in/outcoupling. Integrating near-field refraction into the geometry is thus extremely advantageous. In addition, incorporating an organosilica lens overcomes the shape influence of AuNPs, which always settle with their flat facets face-down onto the mirror (36). These relatively large facets (>20% of the NP diameter) spread out the confined field distribution (30, 37, 38) and lower the maximum field enhancement that can be attained. Incorporating the AuNPs into an organosilica nanosphere prevents reorientation, fixing the point of initial contact, and as a result the faceting now aids formation of down-facing sharp tips and edges that further enhance the optical field (Fig. 1 *A*, *Bottom*).

Experimentally, this dielectric/metallic hybrid nanoarchitecture is realized by synthesizing an organosilica nanosphere onto AuNPs via a nucleation and growth mechanism using a silane coupling agent, 3-methacryloxypropyl-trimethoxysilane (MPTMS) with >90% yield. The MPTMS wetting angle is controlled to be around 50° relative to the AuNP's surface using an amphiphilic polymer (Fig. 1*A* and *SI Appendix*, Fig. S1). The organosilica nanosphere typically has a size polydispersity (p.d.) between 3 and 10% (*SI Appendix*, Fig. S2*A*) and a refractive index of $n = 1.50 \pm 0.01$ (*SI Appendix*, Fig. S2*B*, compared to 1.45 for typical amorphous silica). The resulting dielectric/metallic hybrid colloids (Fig. 1*B*) are deposited onto a gold mirror, forming the geometry depicted in Fig. 1*A*, *Bottom*, henceforth referred to as superefficient plasmonic nanoarchitectures for Raman kinetics' (SPARKs).

To characterize how the submicron spheres affect the optical in/outcoupling of this geometry, finite-difference time-domain (FDTD) simulations are employed. A broadband dipole emitter (*SI Appendix*, Fig. S3) is placed midway between the spherical AuNP and the Au mirror surface and the light emission is modeled over 100 fs, both with and without a nanosphere (*SI Appendix*, *Supplementary Materials and Methods* and Movies V1–V6). At $t = 0.15$ fs, it is clear how the diameter $D = 1{,}000$-nm nanosphere drastically redirects outcoupling away from the surface (Fig. 1*C* and *SI Appendix*, Figs. S4–S6), refracting the far-field emission pattern toward the surface normal. The silica spheres are too small to sustain high-finesse whispering gallery modes, and instead lossy modes are observed. Similar results are found for a dipole emitting at a single wavelength of 703 nm (*SI Appendix*, Fig. S7 and Movies V7 and V8). We term this combination of refraction and leaky surface modes "nanolensing" (submicron spheres being too small to act as a conventional lens for 633-nm light). Full finite-element frequency-domain calculations on facetted (dodecahedral) AuNPs yield similar results and reveal that the embedding depth of the AuNP into the nanolens is also important: As the embedding depth increases from 10 to 70%, the light collection increases by two orders of magnitude for even small 100-nm nanolenses (*SI Appendix*, Fig. S8).

The SPARK nanoarchitectures experimentally yield SERS peak amplitudes exceeding $\sim 10^5$ counts·mW$^{-1}$·s$^{-1}$ (Fig. 1*D*).

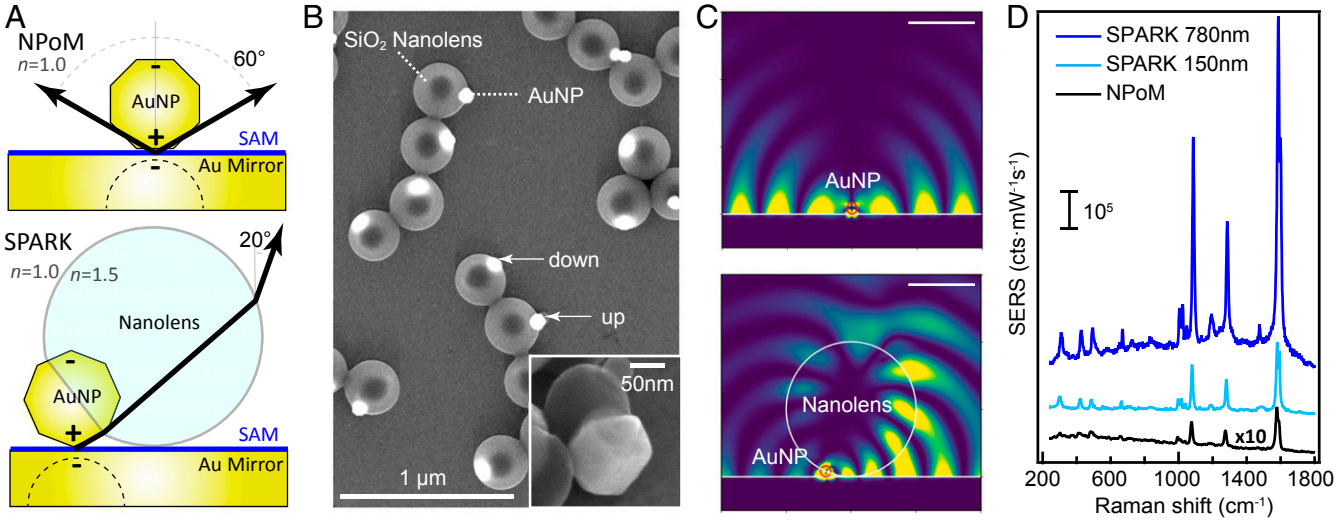


**Fig. 1.** SPARK geometries generate ultrahigh SERS efficiencies. (*A*) Schematic NPoM (*Top*) and SPARK geometries (*Bottom*) with the nanoparticle 50% embedded into the nanolens. Arrows indicate emission angle of the coupled plasmon mode. (*B*) SEM micrographs showing SPARKs on a gold mirror. (*C*) Snapshots of outcoupling broadband light from a local dipole inside the NPoM (*Top*, 80 nm AuNP) and SPARK (*Bottom*, 80 nm AuNP and 800 nm $SiO_2$) geometries, 15 fs after excitation. (Scale bars, 500 nm.) (*D*) Typical SERS spectra for a NPoM and two SPARK geometries with nanolens diameters 150 and 780 nm, using BPT as molecular spacer. NPoM spectrum is scaled ×10 and the spectra vertically offset for clarity.

Even small $D$ = 150-nm optoplasmonic SPARKs yield average optical efficiencies more than an order of magnitude higher than the already powerful conventional NPoM geometry. Larger 780-nm nanolens sizes further raise this efficiency, yielding up to a hundredfold higher intensity than the typical NPoM construct. SERS efficiencies up to $10^7$ counts·mW$^{-1}$·s$^{-1}$ are reached for $D$ = 1,100 nm with an experimental setup optimized for SERS collection (*SI Appendix*, Fig. S10).

**Effect of the Nanolens on SERS Efficiencies.** The FDTD simulations show that with increasing nanolens size the emission angle of the coupled mode for 703-nm light (which is the Stokes wavelength of 1,585-cm$^{-1}$ vibrations from the 633-nm pump) can be redirected from 60° (Fig. 2*A*, gray) to near normal emission (Fig. 2*A*, blue), focusing incident light into and collimating emission out of the hot spot.

Experimentally, the nanolens diameter is controllably grown between $D$ = 150 ± 2 nm (p.d. 7%) and $D$ = 1,100 ± 9 nm (p.d. 2%) simply by varying the amount of MPTMS (Fig. 2*B*). Experimental SERS efficiencies are compared for SPARK diameters ranging from $D$ = 150 nm to 1,100 nm in Fig. 2 *C* and *D*. Note that for SPARKs with a nanolens diameter larger than the diffraction limit, a three-dimensional (3D) optimization step was carried out to locate the position with the highest SERS outcoupling on the SPARK geometry. A clear nonlensing contribution is observed as an immediate 10× gain in signal even for a $D$ = 150-nm nanolens. This can have several different contributions, including symmetry breaking and nanoparticle reorientation. The nanolensing and resonant whispering gallery mode contributions to the SERS efficiency give a linear increase with nanolens size starting from $D$ >390 nm (Fig. 2*D*). These experimental results agree well with the predicted intensities from FDTD simulations (dashed line), which show a sharp increase in SERS intensity compared to NPoMs for small nanolenses and a further gradual increase with nanolens size. Quantitative discrepancies likely arise from locating the dipole emitter in the FDTD simulations only at the central position inside the gap.

Nanolensing is further corroborated experimentally by quantifying the high-angle collection sensitivity, comparing total SERS collected with objectives of numerical aperture (NA) = 0.8 vs. 0.9 (Fig. 2*E*). This ratio quantifies the fraction of high-angle emission (53° vs. 64°), and as the nanolens size is increased the ratio becomes closer to one, showing that the emission is indeed angled closer to the normal. Reciprocally, this also implies that incoupling of light is more tightly focused onto the AuNP, which indeed is observed in 2D real-space SERS mapping of a $D$ = 780-nm SPARK (Fig. 2*F*), where even sub-$\lambda$ translations of

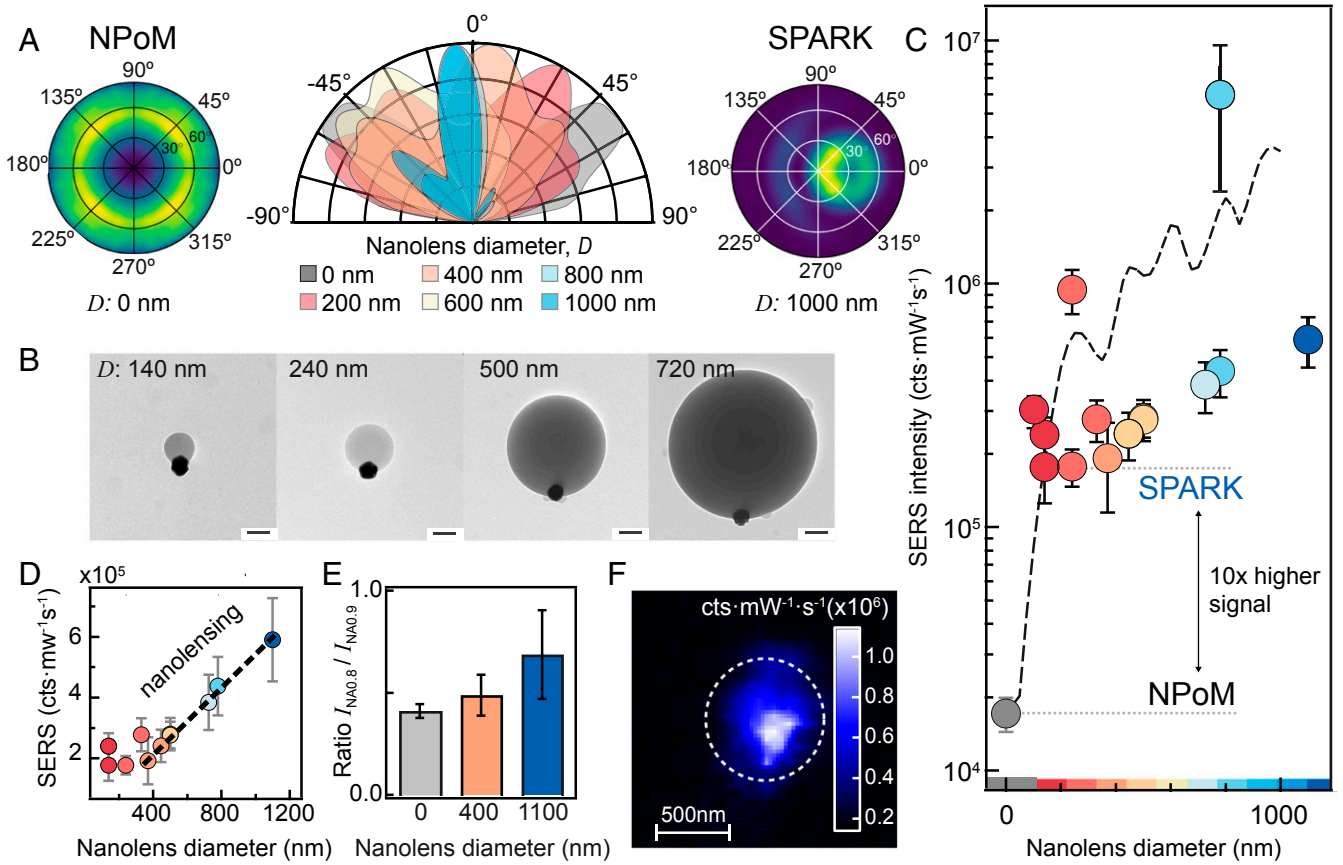


**Fig. 2.** Nanolensing effect in the SERS efficiencies of the SPARK geometry. (*A*) FDTD simulations showing emission angle of a gap-positioned dipole emitter, emitting at 703 nm for different nanolens diameters (*D*) shown in the vertical plane (*Center*) and azimuthal plane (*Left*, NPoM; *Right*, SPARK $D$ = 1,000 nm). (*B*) TEM micrographs of SPARKs of increasing nanolens diameter *D*. (Scale bars, 100 nm.) (*C* and *D*) Averaged SERS intensities for SPARKs of different nanolens diameter [log-scale (*C*), linear-scale (*D*), >20 different spectra averaged per sample, two samples consistently yielded unusually high SERS intensities]. Dashed line denotes predicted SERS intensities for SPARKs based on enhancement factors from FDTD simulations (*SI Appendix*, section 1c). (*E*) High-angle ratio of SERS intensities measured with NA = 0.8 and NA = 0.9 100× objective lenses as a function of nanolens *D*. (*F*) SERS 2D map scan over a SPARK (analyte: BPT, $D$ = 780 nm SPARK, $\lambda_{ex}$ = 633 nm, 1-s integration time, 40 μW); color scale gives SERS intensity of 1,585 cm$^{-1}$ peak, showing localization of SERS signal within SPARK (dashed diameter from dark-field image).

50 nm drastically affect the measured SERS intensity as expected from tight subdiffraction-limited lensing.

To accurately estimate the SERS enhancements reached with these SPARK nanoarchitectures and compare with other systems, the number of molecules probed in the hot spot must be determined. The Janus hybrid changes the contact between the AuNP and mirror from a flat facet to a protruding tip/edge by geometrical constraints, as visible in scanning electron microscopy (SEM) images (Fig. 3*A* and *SI Appendix*, Fig. S11). Therefore, a more strongly confined electromagnetic field is expected than for the NPoM. Earlier studies on nanogap conductance using biphenylthiol (BPT) found ~200 molecules in the active plasmonic volume (39). The geometry of a typical AuNP (icosahedron) suggests that the tip supports a ninefold reduced area compared to the flat facet area from SEM micrographs (*SI Appendix*, Fig. S12); hence, only 22 ± 7 molecules are probed in the SPARK geometry. This in turn implies that the SERS signals of SPARKs stem from ~10 times fewer molecules than in the bare NPoMs, resulting in $8 \times 10^3$ to $3 \times 10^4$ cts·mW$^{-1}$·s$^{-1}$ molecule$^{-1}$ for $D = 150$ nm to 1,100 nm. With an optimized setup, intensities of $5 \times 10^5$ cts·mW$^{-1}$·s$^{-1}$·molecule$^{-1}$ are reached. These measured SERS efficiencies are the highest reported to date (*SI Appendix*, Table T1). Comparing against the Raman signal of an analyte solution, we experimentally determine enhancement factors of $4 \times 10^8$ for NPoMs increasing to $1 \times 10^{11}$ for SPARKs (see calculations in *SI Appendix*, section 5 and Fig. S13).

**High Signal-to-Noise Ratios: Detecting Isotopologues.** The extreme SERS efficiencies from SPARKs open up avenues to a wide range of applications. First, molecular properties that were previously inaccessible can now be probed. Isotopologues are molecules in which at least one constituent atom carries an extra neutron. Artificially synthesized isotopologues have been used for sensing applications as an internal standard (40–42) and to distinguish between few-molecule and single-molecule SERS (SM-SERS) (43, 44). Naturally abundant isotopologues have only been detected in SM-SERS (45, 46), since the isotopologue peak is washed out in average spectrum (45). The exceptional SERS signal-to-noise ratios (>$10^3$: 1 for a 250-μJ laser dose) in our nanoarchitectures allow detection of $^{13}$C isotopologues in the average spectra of nonresonant molecules (Fig. 3*B*). In this way, naturally abundant isotopologues are directly measured in an ensemble of molecules. We use 4′-mercaptobiphenylcarbonitrile (BPT-CN), which has the same structure as BPT but with a cyano group added (18). By natural abundance, the carbon atom located in the cyano triple bond is a $^{13}$C atom in 1.1% of the molecules. Density functional theory calculations predict that the vibrational frequency for the C≡N stretch mode is shifted by −52 cm$^{-1}$ in the BPT-$^{13}$CN, down to 2,154 ± 1 cm$^{-1}$ from 2,206 ± 1 cm$^{-1}$ (*SI Appendix*, section 6). In the SPARK geometry, this C≡N stretching peak is indeed detected above both background and noise in accumulated spectra taken at laser powers <5 μW (Fig. 3 *B*, *Insets*).

The ability to detect this isotope peak enables us to quantify the number of molecules contributing to the SERS signal in the SPARKs. SERS spectra are collected from 36 individual SPARKs, and the percentage of $^{13}$C≡N signal is obtained from the maxima of Gaussians fitted to the $^{13}$C≡N and $^{12}$C≡N peaks. The histogram of occurrences does not show a clear peak at $f = 1.1\%$ but rather displays both lower and higher signal intensities, suggesting fewer than ~100 molecules probed. We numerically model the nanogap using a hexagonal array of points with a lattice spacing of 0.58 nm representing the analyte layer [based on the known spacing of molecules in a biphenyl thiol SAM (47)] and a rotationally symmetric approximation for the electric field distribution in the nanogap (*SI Appendix*, Fig. S14). Each molecule is assigned a 0.011 probability to represent a $^{13}$C isotopologue. For each facet size, 2,000 different realizations of the nanogap are simulated, extracting the $^{13}$C≡N:$^{12}$C≡N SERS intensity ratio for each instance. This yields a histogram of the occurrence frequency of each intensity ratio, for different facet sizes. Comparing the results of this model to the experimental data (Fig. 3*C*), the best fit is found for a facet diameter 10 nm, which agrees reasonably with pentagonal facet size estimates from electron micrographs (8 nm). This supports the notion that the colloidal nanolens orients the AuNP's vertex downward onto the mirror, contributing to the high SERS efficiencies for even small 150-nm SPARKs by way of higher field confinement.

To highlight the versatility of SPARKs and show that such enhanced signals are not unique to BPT or BPT-CN, a range of different analytes are explored including 4-mercaptobenzoic acid (48), *trans*-1,2-bis(4-pyridyl)ethylene (49, 50) and benzenethiol. All these analytes show similar high SERS efficiencies in SPARK geometries (*SI Appendix*, Fig. S15). Rhodamine 6G (R6G) requires laser powers to be below 3 μW for consistent SERS sensing, since R6G is electronically resonant and degrades at even these low laser powers due to the more efficient incoupling of light into the SPARK nanostructure.

**Fast Sensing: Probing Molecular Dynamics at 17-μs Acquisition Times.** The discovery and development of SERS has brought Raman sensing acquisition times down from seconds to milliseconds (18, 34, 51, 52). The greatly increased signals achieved by SPARK nanoarchitectures can now facilitate the collection of SERS spectra at submillisecond integration times, to observe the

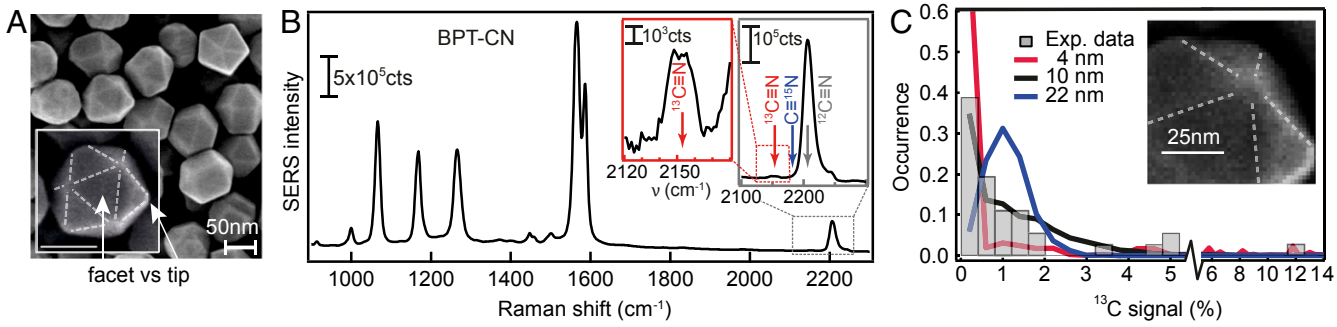


**Fig. 3.** Using the SPARK geometry to detect isotopologues. (*A*) SEM micrograph of AuNPs. (*B*) SERS spectrum for BPT-CN, obtained with $D = 1{,}100$ nm SPARK. Fifty spectra of 1-s integration time were accumulated at low laser power (5 μW) to avoid any molecular damage or gold atom movements. Insets expand peak from $^{13}$C≡N bond. (*C*) Experimental histogram for the occurrence (fraction) of SERS peaks from $^{13}$C≡N bonds (gray) and numerically calculated $^{13}$C≡N SERS intensity percentages for different nanotip diameters (colored). Insets in *A* and *C* show facets outlined (dashed lines) and the AuNP nanotips.

dynamic behavior of molecules at surfaces in more detail. SERS spectra are collected at 10-μs integration times with only 7 μs of dead time (Fig. 4). This unlocks the study of previously inaccessible fast dynamics via real-time monitoring. For example, by pumping plasmonic hotspots with enough laser light, single-atom protrusions or picocavities can be induced that further localize the field down to sub-1-nm$^3$ optical mode volumes (17) (*SI Appendix*, Fig. S16). Picocavities provide an additional several-hundredfold enhancement facilitating single-molecule detection (17, 18). The SPARK system thus allows analysis of the formation dynamics of single-atom protrusions in real-time as Au atoms are pulled out from the gold crystal lattice (Fig. 4 *A*, *Top*). The formation of the picocavity is recognized by the appearance of a set of new Raman lines from the closest bonds (Fig. 4 *A*, *Middle*). Tracking the rise of these lines over time reveals that such a single-atom protrusion is formed over 60 ± 5 μs (at 95% total signal change), in a gradually evolving appearance. Previous studies of adatom movement via electron microscopy or scanning probe microscopy were unable to resolve such timescales, which for this adatom process are seen to be surprisingly slow with atom velocities of ~2 μm·s$^{-1}$. Although the metal adatom movement is found to be light-activated (with 0.8-eV activation energy as expected for adatoms on Au) (17), the high-speed observations here do not correspond to a model of thermal activation over a single barrier of this height.

A second phenomenon observed is the fleeting reconstruction of nanoscale patches on the gold facet surfaces inside the plasmonic hot spot, which are seen as brief local increases in the background SERS signal from free electrons in the metal, which we recently reported (53) and are referred to here as "flares." Even previous high-speed SERS measurements (with 10-ms acquisition times) (18, 34, 53) have averaged over such dynamics, but these can now be clearly resolved (Fig. 4*B*). Averaging the signal between 400 and 1,200 cm$^{-1}$ allows us to fit a flare rise time of 70 ± 5 μs with a similar decay time. The flare timespan of 200 μs is not yet understood and again is much longer than acoustic or thermal timescales in metal nanoparticles. The dynamics after the flare switches off show a brief dip before recovering to a background intensity reduced by a third of that before the flare. This suggests we observe relaxation in the gold crystal lattice as a result of the local surface reconstruction. To ensure that these rise times are not a result of instrument limitations, faster feature changes were identified as well (*SI Appendix*, Fig. S17).

Combining the enhancement from the picocavity with the enhancement from the SPARKs provides sufficient signal to track the motion of single molecules with 17-μs time resolution

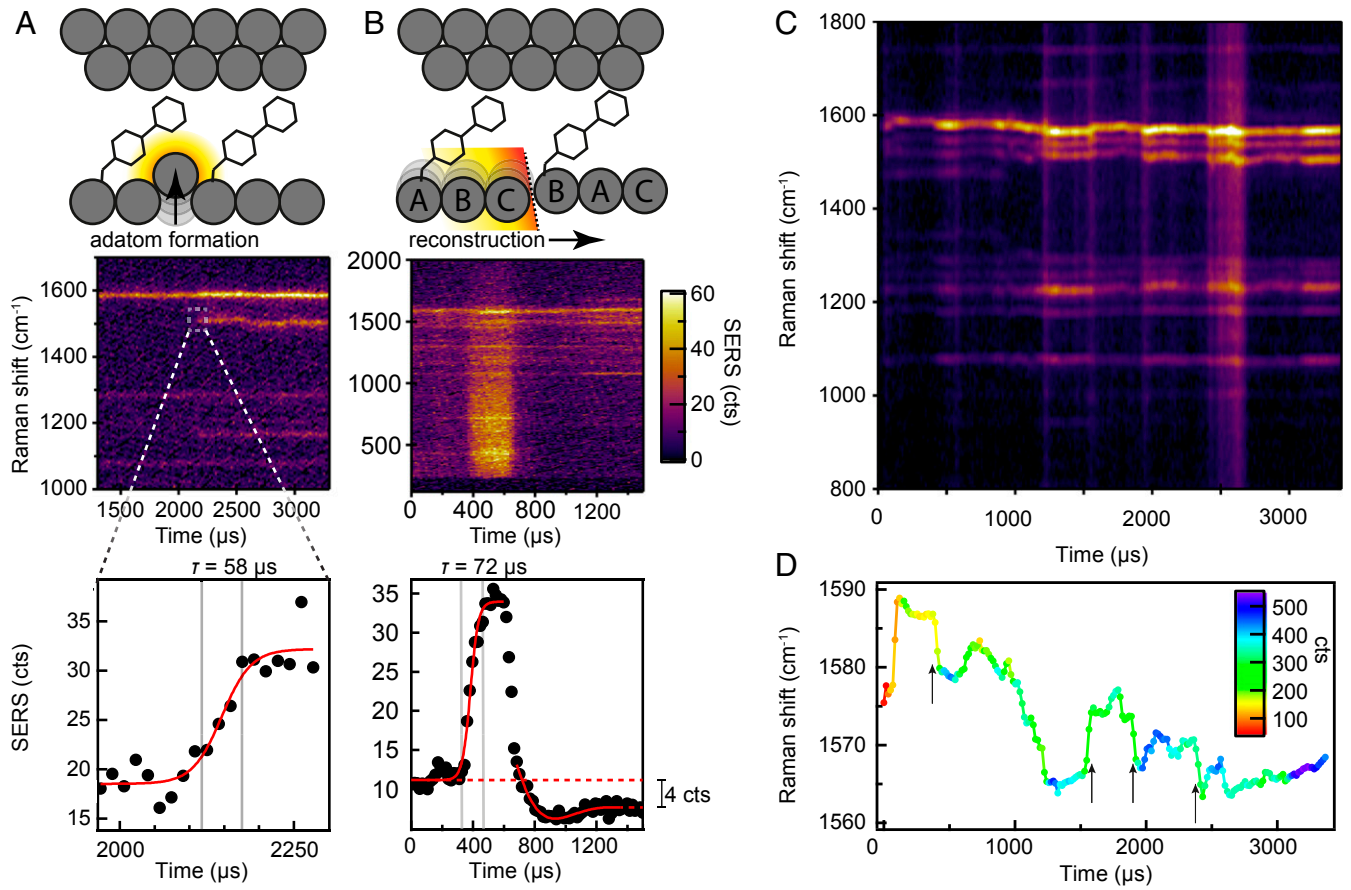


**Fig. 4.** Ultrafast SERS acquisitions with 10-μs integration times (7 μs between spectra) of BPT in a $D$ = 150 nm SPARK geometry from 35-μW laser power using an EMCCD with 50× gain. (*A*) The formation of a picocavity (single Au atom protrusion) tracked in real time. (*A*, *Top*) Scheme depicting atom pullout. (*A*, *Middle*) SERS time scan showing the appearance of new lines at 1,510 cm$^{-1}$ and 1,170 cm$^{-1}$ indicating the formation of a picocavity. (*A*, *Bottom*) SERS intensity during picocavity formation: Measured rise time τ is 60 ± 5 μs (at 95% signal change). (*B*) The formation and destruction of a flare tracked in real time. (*B*, *Top*) Scheme depicting proposed mechanism of flare event (reconstruction of gold lattice). (*B*, *Middle*) SERS time scan showing the rise and fall in SERS background. (*B*, *Bottom*) averaged SERS background showing rise and fall time of flare ~70 ± 5 μs. (*C*) SERS picocavity time scan over 3.4 ms showing the conformational changes of a single molecule with 17-μs time resolution. (*D*) Peak positions of bond in the picocavity vs. time, from *C*, showing that each conformation change is captured by multiple frames even if rapid.

(Fig. 4*C*, *Top*). Under illumination with just enough laser light to induce chemical processes, changes in the peak position are seen, which indicate the molecule is deforming (*SI Appendix*, Fig. S14*D*). Even rapid changes in the vibrational configuration (marked by arrows) are captured (Fig. 4*C*, *Bottom*), demonstrating how such fast molecular dynamics can now fully be tracked in real time using SERS, in addition to the atomic dynamics on metal surfaces.

On account of the ultrafast nature of the Raman emission process and the picosecond relaxation times of the resulting vibrations (54), saturation does not occur here as for fluorescence. Thus, in such a highly optimized SERS substrate, a single nonresonant molecule can be excited far more frequently than a dye or quantum dot. As a result, our nanoarchitecture is able to generate higher photon count rates than conventional single-photon light sources. Integrating the single-molecule signal for a single peak yields integrated count rates between $0.6 \times 10^5$ to $8 \times 10^6$ cts·s$^{-1}$ (*SI Appendix*, Fig. S17), exceeding nearly all single-dye molecule and quantum dot count rates reported to date (*SI Appendix*, Table T2) (19, 20, 55–63). Single-molecule SERS in such an optimized geometry is thus a powerful candidate for single-photon light sources with superior count rates without suffering from blinking or bleaching. Nevertheless, for such devices to be realistically viable, single-atom protrusions will need to be chemically or optically stabilized (17, 18) indefinitely and the single-molecule devices will have to be protected against degradation.

## Conclusions

Several factors aid in the utility of the SPARKs. The high refractive index of the organosilica nanolenses as well as their smooth surfaces (Fig. 2*A*) are beneficial to the nanolensing effect. The submicron-size sphere is lossy, allowing the outcoupled light to radiate rather than being trapped in whispering gallery modes inside the sphere. The partial embedding of AuNPs by ∼ 50% of their diameter into the silica sphere injects the SERS signal directly into the nanolens, without external reflection at the silica/air interface. With the AuNP further outside the nanolens, optical emission reflects from the sphere surface into high-angle directions where it cannot be collected, precluding simple nanoparticle attachment of dielectric spheres to AuNPs. Compared to the 360° torus emitted from nanoparticle dimers, the SPARK emission pattern is still more favorable (63). Interestingly, including a mirror (64, 65) and even a Fabry–Pérot cavity (11) still does not reach the $>5 \times 10^5$ single-molecule counts$^{-1}$·mW$^{-1}$·s$^{-1}$·molecule$^{-1}$ SERS efficiencies observed here.

In summary, these SPARK nanoconstructs embody a versatile sensing platform, which achieves high SERS collection efficiencies produced by a combination of refractive and plasmonic optics. Experimental characterization and full wave simulations show that the incoupling and outcoupling of laser-driven SERS signals from molecules assembled inside the integrated nanogaps is enhanced through the combined effects of nanolensing, reexcitation, and symmetry breaking as well as light concentration through nanoscale reorientation of the AuNP. The measured SERS efficiencies ($10^7$ cts·mW$^{-1}$·s$^{-1}$ and $10^6$ cts·mW$^{-1}$·s$^{-1}$·molecule$^{-1}$) are the highest reported to date. Our results expose avenues to detect trace amounts of analyte molecules, and even naturally abundant isotopes. We show that the extreme efficiencies provided by SPARKs allow us to perform SM-SERS at microsecond integration times, which is of immense value for studying dynamics of materials reconstructions, chemical reactions, and photocatalysis. We demonstrated detection of gold lattice reconstruction and the formation of single-atom protrusions (picocavities) in real time. With count rates of $5 \times 10^5$ to $3 \times 10^7$ s$^{-1}$·molecule$^{-1}$, we showed nonresonant molecules become even brighter than single-molecule dyes (19). Combining this with the improved excitation efficiencies opens up possibilities of using single nonresonant molecules as widespread optical devices.

## Materials and Methods

**Materials.** Gold spheres (diameter 80 nm) stabilized in citrate buffer were purchased from Sigma-Aldrich and used as received. Ammonia solution (35 wt%) was obtained from Fisher Scientific. The following chemicals were purchased from Aldrich: 3-methacryloxypropyltrimethoxysilane (MPTMS, 98%) and 2,2′-azobis(2-methylpropionitrile) (AIBN, 98%). All water was deionized with a Millipore Synergy UV water purification system and has a resistivity of 18.2 MΩ cm. Anhydrous ethanol (<0.003% $H_2O$; Sigma-Aldrich) was used to prepare SAMs of analytes. Analytes used were biphenyl-4-thiol (BPT, 97%; Sigma-Aldrich), 4′-mercaptobiphenylcarbonitrile (BPT-CN, 97%), thiophenol (97%; Merck), 1,2-bis(2-pyridyl)ethylene (97%; Sigma-Aldrich), 4-mercaptobenzoic acid (97%; Sigma-Aldrich), and rhodamine 6G (95%; Sigma-Aldrich). PNIPAM-SH (15 k) was prepared according to ref. 66.

**Gold–Organosilica Heterodimer Synthesis.** Metallic/dielectric hybrid heterodimers were prepared by using AuNPs as seeds for nucleation and growth. Our approach is a version of the reactions presented in refs. 67–69, modified to accommodate AuNPs as seeds. In a typical synthesis, 2 mL of an aqueous solution of PNIPAM-SH (1 g/L) is added to 5 mL of AuNPs. After stirring for 2 h to allow the PNIPAM-SH to adhere to the AuNP surface, excess PNIPAM-SH is washed away by centrifuging the particles three times at 4,000 × *g*, each time replacing the supernatant with 12 mL $H_2O$. By the final centrifugation step, the volume of the dispersion is reduced to 0.3 mL. To grow MPTMS droplets onto the AuNPs, 1 μL ammonia and a chosen amount of MPTMS are added to the dispersion. The reaction mixture is stirred for 2 h at 100 rpm, during which time nucleation and condensation of the MPTMS onto the AuNPs occurs. Subsequently, 2 mg of AIBN is added to the reaction mixture, after which it is placed in a water bath thermostated at 70 °C. This heating step cross-links the methacrylate groups in the MPTMS lobes, creating solid particles. After 2 to 3 h of cross-linking, the reaction is quenched by adding ethanol and the particles are washed by centrifugation in Eppendorf tubes (3,000 rpm). The washing step is repeated at least three times to remove reactants and secondary nuclei. The particles must be stored in ethanol, as hydroxide ions in water etch the MPTMS lobe over time. Note also that PNIPAM-SH adsorption to gold is time-dependent; longer (>12 h) PNIPAM-SH coating of the AuNPs results in fully encapsulated particles. Organosilica sphere sizes as a function of MPTMS concentration are shown in *SI Appendix*, Fig. S2. For example, 3 μL MPTMS results in $D \sim 0.5$-μm organosilica lobes.

**SPARK Sample Preparation.** Samples for SERS measurement (SPARKs) were prepared by depositing gold–organosilica heterodimers onto template-stripped gold (TSG) mirrors decorated with a SAM of analyte. TSG mirrors were prepared as described in ref. 70. BPT was directly dissolved in ethanol to make a 1 mM solution. Pieces of TSG were placed in 2 to 3 mL of this solution and left to form a SAM over 2 d. The gold mirrors were then rinsed with ethanol and dried with nitrogen. Gold–organosilica heterodimers were then deposited from ethanol by placing 60 to 100 μL of dispersion onto a piece of TSG with a SAM. After 10 min, the sample was rinsed with ethanol and dried with $N_2$. For control samples, gold nanospheres were deposited by placing 40 to 60 μL of dispersion in citrate buffer onto a TSG plate with a SAM. After 20 to 30 s, excess particles were rinsed off with water and the samples dried with $N_2$. The deposition time required to reach acceptable surface coverage was longer for SPARKs than for AuNPs, most likely related to a difference in surface charge of organosilica compared to AuNPs.

**SERS Measurements.** Combined SERS and scattering experiments were performed using a modified Olympus BX51 microscope in reflective dark-field geometry. The samples were illumined with a focused white-light source (100-W halogen lamp, angle of incidence of 60°). The dark-field scattered light was analyzed after collection with a fiber-coupled Ocean Optics QE65000 cooled spectrometer. SERS spectra were recorded on a home-built Raman spectrometer coupled into the microscope. A spectrally filtered 632.8-nm helium–neon laser was used as the excitation source. The elastically scattered laser light was filtered with two Semrock 633-nm StopLine single-notch filters. The signal was coupled into an Andor Shamrock i303 spectrograph and Newton electron-multiplying charge-coupled device (EMCCD).

A tightly focused laser spot, near the diffraction limit, is essential for the NPoM geometry, which requires high NA in-coupling. For focusing and collection, three different types of 100× microscope objectives were used. To calculate enhancement factors, an Olympus 0.8 NA objective with long

working distance was used, since the long working distance allows for Raman measurements to be taken from solutions of analytes and compared with SERS from the SPARK substrates. Unless stated otherwise, this 0.8 NA long-working-distance Olympus objective was used for focusing and collection of SERS spectra. To compare the SERS intensities for different NAs (Fig. 2*E*), an Olympus 0.9 NA and a long-working-distance Olympus 0.8 NA objective were used. Finally, for obtaining SERS spectra with optimized counts, a Zeiss 0.9 NA objective was used.

For SPARKs with a nanolens larger than the diffraction limit (i.e., nanolens >300 nm) a 3D optimization step was performed before acquiring spectra, to locate the position where light was optimally coupled into and out of the nanostructure. For SPARKs with a subdiffraction limited nanolens (i.e., nanolens <300 nm), no optimization was necessary other than centering the particle in the laser spot.

**Fast SERS Measurements.** For the fast kinetic measurements, an Andor EMCCD was used with 50× EM gain and a 4.9-μs shift speed. The sample was irradiated with 35-μW laser power. The SERS signal was focused onto a single line on the top of the CCD array and imaged using a "fast kinetics mode" where the image was sequentially shifted down the CCD providing 200 spectra in 3.4 ms. The integration time was set to 10 μs and the read time was 7 μs, resulting in a 17-μs cycle time between spectra. For analysis, SERS spectra were smoothed in wavenumber (but not in time) with a second order 7-point Savitzky–Golay filter.

**FDTD Simulations.** The optical response and far-field emission of the NPoM and SPARK structures were obtained by performing 3D full-wave FDTD simulations using commercial software, Lumerical FDTD version 8.18.1298. The molecular spacer was modeled as a 1.2-nm-thick dielectric material with a refractive index 1.45, and the nanolens (diameter 0 to 1,000 nm) was modeled as a dielectric sphere with refractive index 1.50. The AuNP was modeled as a sphere with a diameter 80 nm which was 50% embedded inside the nanolens. The gold permittivity was taken from Johnson and Christy (71). The simulation domain size was 10 μm × 10 μm × 1.6 μm. We utilized the conformal meshing scheme between dielectric interfaces, but not on metal interfaces, with a maximum step size of 100 nm in all directions. Small mesh refinements of 20 nm, 4 nm, and 0.06 nm were used around the nanolens, AuNP, and spacer, respectively. The nanolensing effect on SERS signals was evaluated in two parts: excitation and emission. For excitation, the structure was excited by a broadband horizontally polarized Gaussian beam with NA = 0.8 which is laterally offset by 100 nm from the center of the AuNP (though other offsets were also tested). For emission, a broadband electric dipole emitter was placed at the middle of the spacer directly below the AuNP. The far-field emission profile was calculated from the recorded fields on a 10-μm × 10-μm monitor located 1.2 μm above the substrate.

**COMSOL Simulations.** Numerical scattering calculations on spatially resolved dodecahedral AuNPs with facet-down configurations were performed using the commercial finite element solver COMSOL Multiphysics Version 5.3a with RF module. The material and geometrical parameters were identical to those used for FDTD simulations above. Angle-resolved far-field Raman scattering was approximated via two successive simulations. First, the NPoM or SPARK system was excited by a background Gaussian beam of 633-nm laser wavelength and microscope NA = 0.8. To accommodate for the strong focusing of the beam we approximated it using a plane wave expansion, that is, a rigorous solution of Maxwell's equations in vacuum, instead of a paraxial representation. The second calculation assumed an excited Raman active BPT molecule in the plasmonic hot spot with isotropic polarizability. This assumption did not strongly influence the results since the plasmonic fields in the nanogap were predominantly z-polarized and thus aligned with the BPT molecules. We used a dipole source of 680-nm wavelength and of current strength proportional to the field at the hot spot to classically emulate the nonlinear quantum mechanical scattering process. Angle-resolved far field power density flow was extracted using the methodology from ref. 72.

**Data Availability Statement.** All relevant data present in this paper can be accessed at the University of Cambridge, https://doi.org/10.17863/CAM.52884. The source data underlying Figs. 1–4 are provided.

**ACKNOWLEDGMENTS.** M.K. thanks the European Commission for a Marie Curie fellowship (Grant 7020005, SPARCLEs) and Peterhouse for a Research Associateship. B.d.N. acknowledges financial support from the Leverhulme Trust through an Early Career Fellowship and from the Newton Trust through matching funding and thanks Hughes Hall for a fellowship. M.K. and B.d.N. are grateful for a Pump Prime grant from the Winton Programme for the Physics of Sustainability. R.C. acknowledges support from Trinity College, University of Cambridge. S.J.B. thanks the European Commission for a Marie Curie fellowship (Grant 658360, NANOSPHERE). O.S.O. acknowledges the support of a Rubicon fellowship from the Netherlands Organisation for Scientific Research. J.J.B. acknowledges support from the Engineering and Physical Sciences Research Council (EPSRC) UK through Grants EP/L027151/1, EP/R020965/1, and NanoDTC EP/L015978/1. O.A.S. acknowledges the ERC-2016 Consolidator Grant (CAM-RIG, 726470) and EPSRC Programme Grant (NOtCH, EP/L027151/1) for funding. O.H. gratefully acknowledges support from the EPSRC through Grants EP/L024926/1 and EP/L027151/1, and from the Science Foundation Ireland (SFI) under Grant 18/RP/6236.

1. H. Yu, Y. Peng, Y. Yang, Z.-Y. Li, Plasmon-enhanced light–matter interactions and applications. *npj Comput. Mater.* **5**, 45 (2019).
2. J. A. Schuller *et al*., Plasmonics for extreme light concentration and manipulation. *Nat. Mater.* **9**, 193–204 (2010).
3. D. Alcaraz Iranzo *et al*., Probing the ultimate plasmon confinement limits with a van der Waals heterostructure. *Science* **360**, 291–295 (2018).
4. S. Gwo, H.-Y. Chen, M.-H. Lin, L. Sun, X. Li, Nanomanipulation and controlled self-assembly of metal nanoparticles and nanocrystals for plasmonics. *Chem. Soc. Rev.* **45**, 5672–5716 (2016).
5. D. Graham *et al*., Theory of SERS enhancement: General discussion. *Faraday Discuss.* **205**, 173–211 (2017).
6. J. Zhang *et al*., Whispering-gallery nanocavity plasmon-enhanced Raman spectroscopy. *Sci. Rep.* **5**, 15012 (2015).
7. I. Alessandri, Enhancing Raman scattering without plasmons: Unprecedented sensitivity achieved by TiO2 shell-based resonators. *J. Am. Chem. Soc.* **135**, 5541–5544 (2013).
8. N. Bontempi, I. Vassalini, S. Danesi, I. Alessandri, ZORRO: Zirconium oxide resonators for all-in-one Raman and whispering-gallery-mode optical sensing. *Chem. Commun. (Camb.)* **53**, 10382–10385 (2017).
9. N. Bontempi, I. Vassalini, I. Alessandri, All-dielectric core/shell resonators: From plasmon-free SERS to multimodal analysis. *J. Raman Spectrosc.* **49**, 943–953 (2018).
10. A. M. Kern *et al*., Enhanced single-molecule spectroscopy in highly confined optical fields: From λ/2-Fabry-Pérot resonators to plasmonic nano-antennas. *Chem. Soc. Rev.* **43**, 1263–1286 (2014).
11. Y. Guo *et al*., Using a Fabry–Perot cavity to augment the enhancement factor for surface-enhanced raman spectroscopy and tip-enhanced Raman spectroscopy. *J. Phys. Chem. C* **122**, 14865–14871 (2018).
12. I. Alessandri, N. Bontempi, L. E. Depero, Colloidal lenses as universal Raman scattering enhancers. *RSC Advances* **4**, 38152–38158 (2014).
13. J. Y. Lee *et al*., Near-field focusing and magnification through self-assembled nanoscale spherical lenses. *Nature* **460**, 498 (2009).
14. Y. Yan *et al*., Microsphere-coupled scanning laser confocal nanoscope for sub-diffraction-limited imaging at 25 nm lateral resolution in the visible spectrum. *ACS Nano* **8**, 1809–1816 (2014).
15. H. Zhu, B. Yan, S. Zhou, Z. Wang, L. Wu, Synthesis and super-resolution imaging performance of a refractive-index-controllable microsphere superlens. *J. Mater. Chem. C Mater. Opt. Electron. Devices* **3**, 10907–10915 (2015).
16. B. Hou *et al*., Microsphere assisted super-resolution optical imaging of plasmonic interaction between gold nanoparticles. *Sci. Rep.* **7**, 13789 (2017).
17. F. Benz *et al*., Single-molecule optomechanics in "picocavities". *Science* **354**, 726–729 (2016).
18. C. Carnegie *et al*., Room-temperature optical picocavities below 1 $nm^3$ accessing single-atom geometries. *J. Phys. Chem. Lett.* **9**, 7146–7151 (2018).
19. B. Lounis, W. E. Moerner, Single photons on demand from a single molecule at room temperature. *Nature* **407**, 491–493 (2000).
20. N. Somaschi *et al*., Near-optimal single-photon sources in the solid state. *Nat. Photonics* **10**, 340 (2016).
21. J. J. Baumberg, J. Aizpurua, M. H. Mikkelsen, D. R. Smith, Extreme nanophotonics from ultrathin metallic gaps. *Nat. Mater.* **18**, 668–678 (2019).
22. G.-C. Li, Q. Zhang, S. A. Maier, D. Lei, Plasmonic particle-on-film nanocavities: A versatile platform for plasmon-enhanced spectroscopy and photochemistry. *Nanophotonics* **7**, 1865–1889 (2018).
23. J. Mertens *et al*., Controlling subnanometer gaps in plasmonic dimers using graphene. *Nano Lett.* **13**, 5033–5038 (2013).
24. M.-E. Kleemann *et al*., Strong-coupling of $WSe_2$ in ultra-compact plasmonic nanocavities at room temperature. *Nat. Commun.* **8**, 1296 (2017).
25. R. W. Taylor *et al*., Watching individual molecules flex within lipid membranes using SERS. *Sci. Rep.* **4**, 5940 (2014).
26. T. Ding *et al*., Controllable tuning plasmonic coupling with nanoscale oxidation. *ACS Nano* **9**, 6110–6118 (2015).
27. C. Readman *et al*., Anomalously large spectral shifts near the quantum tunnelling limit in plasmonic rulers with subatomic resolution. *Nano Lett.* **19**, 2051–2058 (2019).

28. M. Hu, A. Ghoshal, M. Marquez, P. G. Kik, Single particle spectroscopy study of metal-film-induced tuning of silver nanoparticle plasmon resonances. *J. Phys. Chem. C* **114**, 7509–7514 (2010).
29. C. Lumdee, B. Yun, P. G. Kik, Wide-band spectral control of Au nanoparticle plasmon resonances on a thermally and chemically robust sensing platform. *J. Phys. Chem. C* **117**, 19127–19133 (2013).
30. C. Tserkezis *et al*., Hybridization of plasmonic antenna and cavity modes: Extreme optics of nanoparticle-on-mirror nanogaps. *Phys. Rev. A* **92**, 53811 (2015).
31. B. de Nijs *et al*., Unfolding the contents of sub-nm plasmonic gaps using normalising plasmon resonance spectroscopy. *Faraday Discuss.* **178**, 185–193 (2015).
32. D. O. Sigle *et al*., Observing single molecules complexing with cucurbit[7]uril through nanogap surface-enhanced Raman spectroscopy. *J. Phys. Chem. Lett.* **7**, 704–710 (2016).
33. R. Chikkaraddy *et al*., Single-molecule strong coupling at room temperature in plasmonic nanocavities. *Nature* **535**, 127–130 (2016).
34. B. de Nijs *et al*., Plasmonic tunnel junctions for single-molecule redox chemistry. *Nat. Commun.* **8**, 994 (2017).
35. R. Chikkaraddy *et al*., How ultranarrow gap symmetries control plasmonic nanocavity modes: From cubes to spheres in the nanoparticle-on-mirror. *ACS Photonics* **4**, 469–475 (2017).
36. D. O. Sigle *et al*., Monitoring morphological changes in 2D monolayer semiconductors using atom-thick plasmonic nanocavities. *ACS Nano* **9**, 825–830 (2015).
37. N. Kongsuwan, A. Demetriadou, R. Chikkaraddy, J. J. Baumberg, O. Hess, Fluorescence enhancement and strong-coupling in faceted plasmonic nanocavities. *EPJ Appl. Metamat.* **5**, 6 (2018).
38. Y. Huang, L. Ma, J. Li, Z. Zhang, Nanoparticle-on-mirror cavity modes for huge and/or tunable plasmonic field enhancement. *Nanotechnology* **28**, 105203 (2017).
39. F. Benz *et al*., Generalized circuit model for coupled plasmonic systems. *Opt. Express* **23**, 33255–33269 (2015).
40. R. Goodacre, D. Graham, K. Faulds, Recent developments in quantitative SERS: Moving towards absolute quantification. *Trends Analyt. Chem.* **102**, 359–368 (2018).
41. A. Subaihi *et al*., Quantitative detection of codeine in human plasma using surface-enhanced Raman scattering via adaptation of the isotopic labelling principle. *Analyst* **142**, 1099–1105 (2017).
42. A. Subaihi *et al*., Towards improved quantitative analysis using surface-enhanced Raman scattering incorporating internal isotope labelling. *Anal. Methods* **9**, 6636–6644 (2017).
43. J. A. Dieringer, R. B. Lettan 2nd, K. A. Scheidt, R. P. Van Duyne, A frequency domain existence proof of single-molecule surface-enhanced Raman spectroscopy. *J. Am. Chem. Soc.* **129**, 16249–16256 (2007).
44. A. B. Zrimsek, N. L. Wong, R. P. Van Duyne, Single molecule surface-enhanced raman spectroscopy: A critical analysis of the bianalyte versus isotopologue proof. *J. Phys. Chem. C* **120**, 5133–5142 (2016).
45. P. G. Etchegoin, E. C. Le Ru, M. Meyer, Evidence of natural isotopic distribution from single-molecule SERS. *J. Am. Chem. Soc.* **131**, 2713–2716 (2009).
46. C. G. Artur, R. Miller, M. Meyer, E. C. Le Ru, P. G. Etchegoin, Single-molecule SERS detection of C60. *Phys. Chem. Chem. Phys.* **14**, 3219–3225 (2012).
47. D. G. Matei, H. Muzik, A. Gölzhäuser, A. Turchanin, Structural investigation of 1,1′-biphenyl-4-thiol self-assembled monolayers on Au(111) by scanning tunneling microscopy and low-energy electron diffraction. *Langmuir* **28**, 13905–13911 (2012).
48. A. Michota, J. Bukowska, Surface-enhanced Raman scattering (SERS) of 4-mercaptobenzoic acid on silver and gold substrates. *J. Raman Spectrosc.* **34**, 21–25 (2003).
49. W. Yang, J. Hulteen, G. C. Schatz, R. P. Van Duyne, A surface-enhanced hyper-Raman and surface-enhanced Raman scattering study of trans-1,2-bis(4-pyridyl)ethylene adsorbed onto silver film over nanosphere electrodes. Vibrational assignments: Experiment and theory. *J. Chem. Phys.* **104**, 4313–4323 (1996).
50. E. A. Sprague-Klein *et al*., Photoinduced plasmon-driven chemistry in trans-1,2-Bis(4-pyridyl)ethylene gold nanosphere oligomers. *J. Am. Chem. Soc.* **140**, 10583–10592 (2018).
51. C. Zong, C.-J. Chen, M. Zhang, D.-Y. Wu, B. Ren, Transient electrochemical surface-enhanced raman spectroscopy: A millisecond time-resolved study of an electrochemical redox process. *J. Am. Chem. Soc.* **137**, 11768–11774 (2015).
52. A. J. Wain, M. A. O'Connell, Advances in surface-enhanced vibrational spectroscopy at electrochemical interfaces. *Adv. Phys. X* **2**, 188–209 (2017).
53. C. Carnegie *et al*., Flickering nanometre-scale disorder in a crystal lattice tracked by plasmonic flare light emission. *Nat. Commun.* **11**, 682 (2020).
54. N.-H. Seong, Y. Fang, D. D. Dlott, Vibrational energy dynamics of normal and deuterated liquid benzene. *J. Phys. Chem. A* **113**, 1445–1452 (2009).
55. S. Strauf *et al*., High-frequency single-photon source with polarization control. *Nat. Photonics* **1**, 704 (2007).
56. A. Renn, J. Seelig, V. Sandoghdar, Oxygen-dependent photochemistry of fluorescent dyes studied at the single molecule level. *Mol. Phys.* **104**, 409–414 (2007).
57. G. Wrigge, I. Gerhardt, J. Hwang, G. Zumofen, V. Sandoghdar, Efficient coupling of photons to a single molecule and the observation of its resonance fluorescence. *Nat. Phys.* **4**, 60–66 (2008).
58. J. Claudon *et al*., A highly efficient single-photon source based on a quantum dot in a photonic nanowire. *Nat. Photonics* **4**, 174–177 (2010).
59. B. Pradhan *et al*., Gold-nanorod-enhanced fluorescence correlation spectroscopy of Fluorophores with high quantum yield in lipid bilayers. *J. Phys. Chem. C* **120**, 25996–26003 (2016).
60. D. Wang *et al*., Coherent coupling of a single molecule to a scanning Fabry-Perot microcavity. *Phys. Rev. X* **7**, 21014 (2017).
61. K. Matsuzaki *et al*., Strong plasmonic enhancement of biexciton emission: Controlled coupling of a single quantum dot to a gold nanocone antenna. *Sci. Rep.* **7**, 42307 (2017).
62. W. Zhang, M. Caldarola, X. Lu, M. Orrit, Plasmonic enhancement of two-photon-excited luminescence of single quantum dots by individual gold nanorods. *ACS Photonics* **5**, 2960–2968 (2018).
63. C. U. Hail *et al*., Nanoprinting organic molecules at the quantum level. *Nat. Commun.* **10**, 1880 (2019).
64. G.-C. Li, Y.-L. Zhang, J. Jiang, Y. Luo, D. Y. Lei, Metal-substrate-mediated plasmon hybridization in a nanoparticle dimer for photoluminescence line-width shrinking and intensity enhancement. *ACS Nano* **11**, 3067–3080 (2017).
65. G.-C. Li, Y.-L. Zhang, D. Y. Lei, Hybrid plasmonic gap modes in metal film-coupled dimers and their physical origins revealed by polarization resolved dark field spectroscopy. *Nanoscale* **8**, 7119–7126 (2016).
66. S. T. Jones *et al*., The importance of excess poly(N-isopropylacrylamide) for the aggregation of poly(N-isopropylacrylamide)-coated gold nanoparticles. *ACS Nano* **10**, 3158–3165 (2016).
67. S. Sacanna, L. Rossi, D. J. Pine, Magnetic click colloidal assembly. *J. Am. Chem. Soc.* **134**, 6112–6115 (2012).
68. S. Sacanna *et al*., Shaping colloids for self-assembly. *Nat. Commun.* **4**, 1688 (2013).
69. M. Kamp *et al*., Regiospecific nucleation and growth of silane coupling agent droplets onto colloidal particles. *J. Phys. Chem. C Nanomater Interfaces* **121**, 19989–19998 (2017).
70. F. Benz *et al*., Nanooptics of molecular-shunted plasmonic nanojunctions. *Nano Lett.* **15**, 669–674 (2015).
71. P. B. Johnson, R. W. Christy, Optical constants of the noble metals. *Phys. Rev. B* **6**, 4370–4379 (1972).
72. J. Yang, J.-P. Hugonin, P. Lalanne, Near-to-far field transformations for radiative and guided waves. *ACS Photonics* **3**, 395–402 (2016).